IEEE Access
Multidisciplinary | Rapid Review | Open Access Journal

Received November 22, 2019, accepted January 8, 2020, date of publication January 14, 2020, date of current version January 27, 2020.

Digital Object Identifier 10.1109/ACCESS.2020.2966528

Design of a Cable-Driven Auto-Charging Robot for Electric Vehicles

YA'NAN LOU AND SHICHUN DI
School of Mechatronics Engineering, Harbin Institute of Technology, Harbin 150001, China
Corresponding author: Shichun Di (dishichun@sharee.net)

ABSTRACT With the increasing popularity of electric vehicles, low level of automation for charging process has become one of the main factors restricting the development of electric vehicles. Recently, auto-charging robots which have the ability to transform manual process plugging charging plugs into charging ports to automatic plugging-unplugging operation have arisen. This paper presents a 4-DOF cable-driven auto-charging robot (CDACR) consisting of a 3-DOF cable-driven serial manipulator (CDSM) and a moving platform. In this design, the 3-DOF CDSM is actuated by six cables being routed through five disks fixed to the CDSM's rigid links. The end-effector of CDACR is a flexible plug that has the ability to withstand small elastic deformation. The control algorithm and the plugging-unplugging strategy were designed to respond to various parking situations with or without yaw error. This paper takes the lead in introducing the cable-driven robot into the field of automatic charging. Besides, through simulated charging experiments, the feasibility and effectiveness of using CDACR to realize auto-charging for electric vehicles has been demonstrated.

INDEX TERMS Cable-driven robot, auto-charging robot, electric vehicles.

I. INTRODUCTION

Electric vehicles are rapidly becoming popular on our roads. Presently, the charging process still depends on manual operation [1]. In other words, the connection between charging plugs and charging ports of electric vehicles has to be realized by users. The inconvenience and low level of automation have seriously limited the extension of electric vehicles. The robotic auto-charging device provides an attractive solution to the above problem, as shown in Fig. 1.

Depending on the type of robots used, current robotic automatic charging devices for the electric vehicles can be broadly classified into the following three categories: 1) traditional articulated manipulators, 2) AGV, 3) bionic manipulator. Devices of the first category include Volkswagen e-smart Connect based on a KUKA LBR iiwa [1], the Robotic Charging Station based on UR10 robot developed by Graz University of Technology [2], and PowerHydrant [3]. These designs based on traditional articulated manipulators and were capable of automatically plugging and unplugging vehicle connectors to electric vehicles. However, technical details on positioning error of charging ports, the adaptability for different types of charging ports, and the consume time of single plugging-unplugging have not yet been made public. Devices of the second category include Samsung's robot charging unit EVAR [4]. This design can move to electric vehicle being parked anywhere and connect to charge automatically. However, this design need users to attach a special EVSE adapter to the number plate manually. Devices of the third category include Tesla charging-robot based on a concept of a snake-like robot [5]. This design was able to locate charging ports and then use bionic snakelike robots to plug in electric vehicles automatically. However, the actuation method and detailed technical information have not been

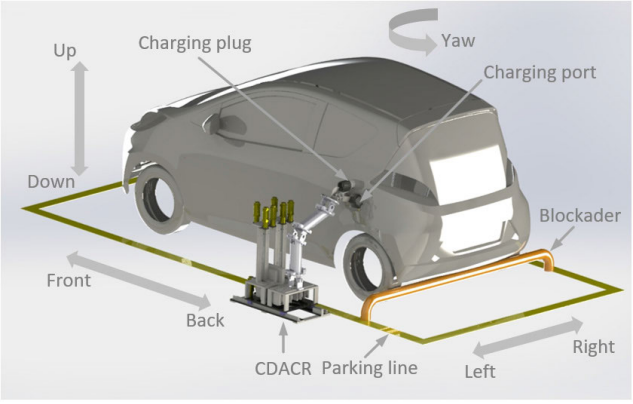

FIGURE 1. CAD model of the robotic auto-charging concept.

The associate editor coordinating the review of this manuscript and approving it for publication was Yongping Pan.

found in literature yet. This paper focuses on robotic auto-charge devices belonging to the third category of designs.

Some limitations and difficulties of auto-charging robot designs are the following.

1) The robots are required to cope with various vehicles types and corresponding positions of charging sockets [6].
2) The robots are required to cope with as large parking error as possible.
3) The robots are required to deal with complex parking situations in practical application, for example, the change of the charging port poses during the charging process due to drivers getting on or off vehicles.
4) The robots are required to hand and manage the charging cables, especially the cables used by DC quick charging [6].
5) The robots are required to possess high compliance to prevent charging ports and robots from damaging in the event of impacts with human or vehicles and contact force between robots and charging ports exceeding a given threshold.

A cable-driven serial manipulator (CDSM) is featured of a series of connected rigid bodies being driven by cables instead of actuators positioned at each joint [7]. Thus, CDSMs process low stiffness, light-weight structure, low moving mass, and large reachable workspace [8]–[10]. These advantages are desirable in robotic auto-charging devices. Thus, cable-driven was chosen as the actuation type of the auto-charging robot proposed in this paper. The design [11]–[20], modelling [21]–[23], and control [24]–[28] for CDSM in actual application and basic theory have been studied by some researches. The optimization design work of attachment points and the mechanical structure parameters for various objective functions were shown in [11], [12], [18], [19] and [13], [14], [15], [16], [17], [20], respectively. The general model of CDSM was investigated systematically by [21]–[23]. Positive cable tension is the basis of the control of cable-driven robots. There are a lot of relevant literatures to solve this problem. The work in [24]–[28] is typical among those literatures. To the authors' knowledge, little research on robotic auto-charging devices based on CDSM has been done. In this paper, a 4-DOF cable-driven auto-charging robot (CDACR) consisting of a 3-DOF CSDM and a moving platform is developed. Six cables were used to control the 3-DOF CDSM. The slackness of these cables was avoided, which achieves high positioning accuracy and load capacity. The flexible plug was designed to reduce the requirement for positioning accuracy and provide high compliance. Deflected links were designed to reduce the joint limits because large joint limits will increase the possibility of cable slackness.

The merits of CDACR are the following.

1) The DOF number of CDACR is only four. However, the combination of CDACR and the flexible plug has the ability to complete a real charging task.
2) The ingress protection (IP) level of CDACR is high because the motors moved to the robot base are easily protected, which can adapt to more complex actual auto-charging scenarios than those devices based on traditional articulated manipulators.
3) The economic cost of the proposed CDSM is low due to the absence of expensive reducer positioned at each joint.
4) The designed CDSM (11.0 kg) is far lighter than UR10 robot (28.9 kg) and KUKA LBR iiwa (30 kg) due to the rear motors and the absence of reducer positioned at each joint.

The innovation of this paper lies in:

1) Introducing the cable-driven robot into the field of automatic charging for electric vehicles firstly.
2) Completing the design, modelling and control of a 4-DOF CDACR with a flexible plug.
3) Proposing the auto-charging robot based on cable-driven possessing obvious merits compared to the existing auto-charging device.
4) Being the first to carry out the plugging-unplugging test under arbitrary poses of charging ports, publishing experimental results, and verifying the feasibility and effectiveness of using cable-driven robot to realize auto-charging for electric vehicles.

With the development of stereo garages and intelligent parking, manually operating charging plugs is no longer compatible with high level of automation. Automatic charging is the general trend. The work of this paper is very meaningful for the development of electric vehicles and social transport.

This paper is organized as follows: Section II presents the optimization design, sensing and actuation. Section III presents the kinematic and dynamic modelling of CDACR. Section IV constructs the plugging-unplugging controller and strategy. Section V designs the experiment and presents experimental results including the trajectory tracking accuracy, positioning accuracy, cable tensions, and plugging-unplugging forces/torques. This paper is finally concluded in Section VI.

II. AUTO-CHARGING ROBOT DESIGN

A. MECHANICAL DESIGN

1) DOF DISTRIBUTION AND LINK DESIGN

According to the actual charging requirements, 4-DOF CDACR was designed. This robot consists of two parts, i.e., a 3-DOF cable-driven manipulator and a moving platform.

The detailed definition of link frames for CDACR is shown in Fig. 2. As shown in Fig. 2, the CDSM of the auto-charging robot consists of three DOFs and these corresponding revolute axes are all parallel. The moving platform provides translational motion along the front/back direction (as shown in Fig. 1) of the vehicle. To reduce the joint limits of CDSM during the plugging-unplugging process, the links of CDSM were designed with deflection angles. This makes the description of one link requires three length parameters and two

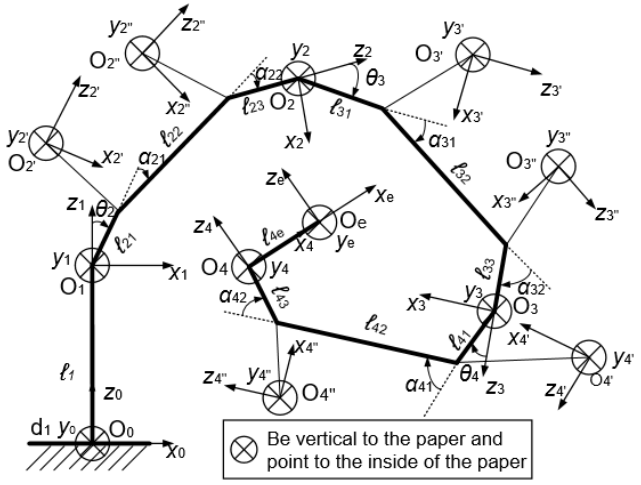

FIGURE 2. Link frames of the designed 4-DOF cable-driven auto-charging robot.

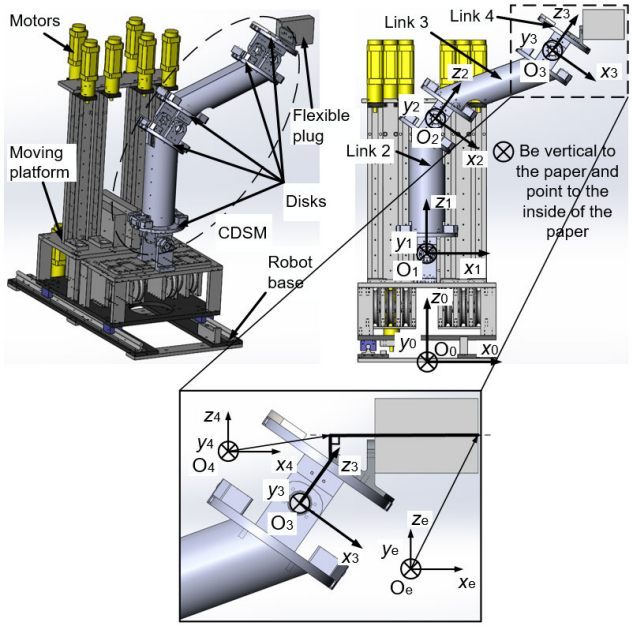

FIGURE 3. CAD model of the 4-DOF CDACR.

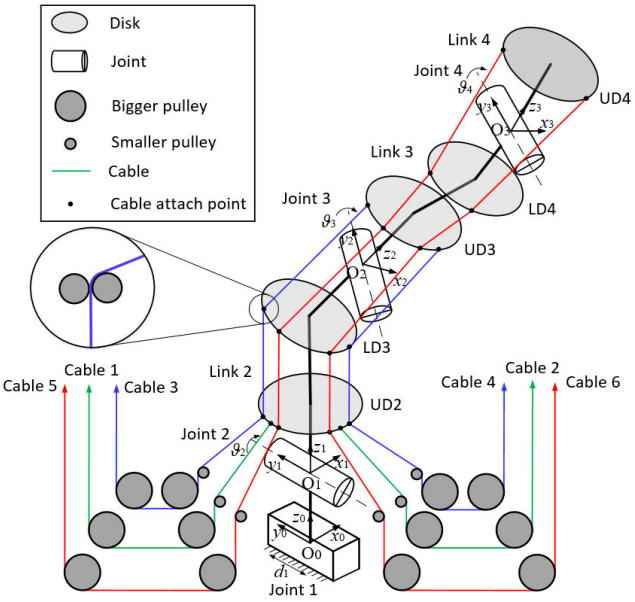

FIGURE 4. Cable routing path of CDACR.

angle parameters. The link parameters will be optimized in Section II. C.

The coordinate frames O_0 to O_4 and O_e are attached to the robot base, the moving platform, link 2 to link 4, and the flexible plug, respectively. The coordinate frames from $O_{2'}$, $O_{2''}$ to $O_{4'}$, $O_{4''}$ are the second and third frame attached to link 2 to link 4, respectively. The origins of these frames coincide with the deflect points of the deflected links. Symbol ℓ_1 denotes the height of the first rotating joint from the ground. Symbols ℓ_{i1}, ℓ_{i2} and ℓ_{i3} $(i = 2, 3, 4)$ denote the link lengths of link i. Symbols α_{i1} and α_{i2} $(i = 2, 3, 4)$ denote the deflection angles of link i. The symbol l_{4e} denotes the length of the flexible plug. The joint space for the entire system can be represented by $\boldsymbol{q} = \begin{bmatrix} d_1 & \theta_2 & \theta_3 & \theta_4 \end{bmatrix}^T \in \mathbb{R}_{4\times 1}$.

The optimized CDACR using the optimization method illustrated in Section II. C is shown in Fig. 3. Its end-effector is a flexible plug which is fixed to Link 4 by elastic element. Due to the presence of the elastic element, the flexible plug can withstand small rotational elastic deformation around three mutually perpendicular axes. The robot links were designed to be hollow so that the charging cables can easily route along the inside of these links.

The DOF distribution of CDACR is enough for a real charging task. The reasons are shown in the following. CDSM provides two translational motion along the left/right and up/down directions of electric vehicles and one rotational motion about the front/back direction of electric vehicles. The moving platform provides the translational motion along the front/back direction of electrical vehicles. Simultaneously, the flexible plug provides small rotational motion about three mutually perpendicular axes. Therefore, the 3-DOF CDSM, the moving platform, and the flexible plug together have the ability to complete the task of positioning and orienting the flexible plug.

2) CABLE ROUTING PATH DESIGN

CDACR consists of five disks: the second joint upper disk (UD2, located on link 2), the third joint lower disk (LD3, located on link 2) and upper disk (UD3, located on link 3), and the fourth joint lower disk (LD4, located on link 3) and upper disk (UD4, located on link 4), as shown in Fig. 4. These disks were designed for cable-routing.

Six cables are routed through these disks to drive the robot. The first two cables numbered 1 and 2 are routed through the moving platform (the base of CDSM) and terminate on the second joint upper disk (UD2). They control the clockwise and counterclockwise motion of the first revolute joint. The second two cables numbered 3 and 4 are routed through the moving platform, the second joint upper disk

(UD2), the third joint lower disk (LD3) and, eventually, terminate on the third joint upper disk (UD3). They control the clockwise and counterclockwise motion of the second revolute joint. The last two cables numbered 5 and 6 are routed through the moving platform, the second joint upper disk (UD2), the third joint lower disk (LD3), the third joint upper disk (UD3), and the fourth joint lower disk (LD4) and, eventually, terminate on the third joint upper disk (UD4). They control the clockwise and counterclockwise motion of the third revolute joint.

The requirement of a minimum of $n + 1$ cables for an n-DOF cable-driven open chain have been mathematically proven [29]. It has been proven that the volume of the ''tensioned'' workspace can be improved by the additional cables in the system [8]. In this paper, six cables are used to actuate three DOFs. This satisfies the minimum cable requirement in the system. Moreover, these redundant cables are expected to aid in regulating stiffness. This is crucial for a cable-driven auto-charging robot.

Due to the reasonable distribution of the cable attachment points, these cables are routed through different paths, which prevents interference between cables and between cables and robot during the robot motion. The cable attachment points are essential kinematic parameters which directly affect the kinematical model between joint space and cable space. Pulleys were applied in these cable attachment points where relative motion between cables and robot occurs, as shown in Fig. 4. This reduces the friction between cables and robot, thereby lower the actuator torque and meanwhile increase the cable bend radius. This transforms the resisting force between cables and robot from sliding friction into rolling friction.

B. SENSING, ACTUATION, AND CONTROL

An encoder is mounted at each joint of the CDSM to measure the joint angles in real time, which will be later used in closed-loop feedback control of the desired motion. Seven PMSM motors are used to drive the auto-charging robot. One motor placed on the robot base drives the moving platform. Other six ones placed on the moving platform drive the CDSM, as shown in Fig. 3. The motors can be run in position, velocity, and torque mode. The ball screw pairs are used to convert the rotational motion of the motors into the translational motion (elongation and shortening) of the cables. Stainless steel or dyneema cables are used to actuate the CDSM. Between the first two bigger pulleys, as shown in Fig. 4, a load cell is attached for each cable. It measures the cable tension, but it cannot be used for closed-loop feedback control due to its poor real-time performance. Vision sensor is used to measure the poses of charging ports. ATI F/T sensor is used to measure the interaction forces/torques during plugging-unplugging process. An IPC (Industry Personal Computer) is used to integrate the information from the joint encoders, motors, load cells and vision sensor, and then carry out the control of the robot. A PC desktop is used to provide a user interface and carry out the remote control of the IPC control system.

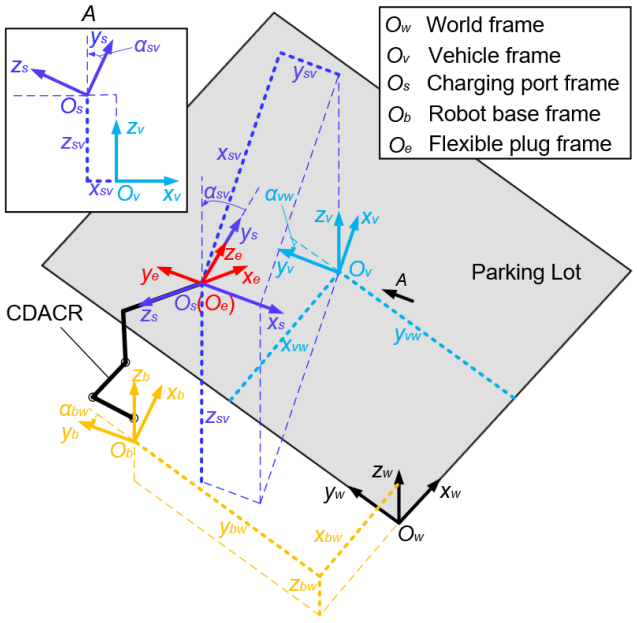

FIGURE 5. General parking situation based on parking lot described by five frames.

C. PLUGGING-UNPLUGGING WORKSPACE OPTIMIZATION

1) MATHEMATICALIZATION OF AUTOMATIC CHARGING SCENE

Figure 5 shows a general parking situation including the resulting pose of the charging port and the corresponding charging solution realized by CDACR. To describe the entire auto-charging scene mathematically, five frames are established, including the world frame O_w, vehicle frame O_v, charging port frame O_s, robot base frame O_b, and flexible plug frame O_e.

Therefore, the homogeneous transformations $\boldsymbol{T}_v^w$, $\boldsymbol{T}_b^w$ and $\boldsymbol{T}_s^v$ describe the position and orientation of the vehicle frame with respect to the world frame, of the robot base frame with respect to the world frame and of the charging port frame with respect to the vehicle frame, respectively. The transformation $\boldsymbol{T}_v^w$ describes the generalized parking situation with left/right, front/back, and yaw parking errors. The transformation $\boldsymbol{T}_b^w$ describes the installation of CDACR. The transformation $\boldsymbol{T}_s^v$ is a constant that describes the detailed position and orientation of the charging port with respect to vehicle and depends on the vehicle type. How to design and install the auto-charging robot directly affects the size of the plugging-unplugging workspace. Hence, the plugging-unplugging workspace must be optimized to ensure the adaption with as large parking error as possible. The corresponding pose of the charging port with respect to the world frame can be computed by the matrix multiplication $\boldsymbol{T}_v^w \boldsymbol{T}_s^v$. The detailed forms of $\boldsymbol{T}_v^w$, $\boldsymbol{T}_b^w$ and $\boldsymbol{T}_s^v$ are shown in the following:

$$\boldsymbol{T}_v^w = \begin{bmatrix} \cos\alpha_{vw} & -\sin\alpha_{vw} & 0 & x_{vw} \\ \sin\alpha_{vw} & \cos\alpha_{vw} & 0 & y_{vw} \\ 0 & 0 & 1 & 0 \\ 0 & 0 & 0 & 1 \end{bmatrix},$$

$$\boldsymbol{T}_b^w = \begin{bmatrix} \cos\alpha_{bw} & -\sin\alpha_{bw} & 0 & x_{bw} \\ \sin\alpha_{bw} & \cos\alpha_{bw} & 0 & y_{bw} \\ 0 & 0 & 1 & z_{bw} \\ 0 & 0 & 0 & 1 \end{bmatrix},$$

$$\boldsymbol{T}_s^v = \begin{bmatrix} 0 & 0 & -1 & x_{sv} \\ -\cos\alpha_{sv} & \sin\alpha_{sv} & 0 & y_{sv} \\ \sin\alpha_{sv} & \cos\alpha_{sv} & 1 & z_{sv} \\ 0 & 0 & 0 & 1 \end{bmatrix},$$

where x_{vw}, y_{vw} and α_{vw} denote the coordinates of the origin of vehicle frame O_v with respect to the world frame O_w and the rotation angle about axis z_w, respectively; x_{bw}, y_{bw}, z_{bw} and α_{bw} denote the coordinates of the origin of robot base frame O_b with respect to the world frame O_w, and the rotation angle about axis z_w, respectively; x_{sv}, y_{sv}, z_{sv} and α_{sv} denote the coordinates of the origin of the charging port frame O_s with respect to the vehicle frame O_v and the rotation angle about axis z_v, respectively.

The pose of the charging port frame O_s with respect to the robot base frame O_b is computed by

$$\boldsymbol{T}_s^b = \left(\boldsymbol{T}_b^w\right)^{-1} \boldsymbol{T}_v^w \boldsymbol{T}_s^v \tag{1}$$

In the plugging position, as shown in Fig. 5, the pose of the charging port frame O_s with respect to the flexible plug frame O_e can be expressed as

$$\boldsymbol{T}_s^e = \begin{bmatrix} 0 & 0 & -1 & 0 \\ -1 & 0 & 0 & 0 \\ 0 & 1 & 0 & 0 \\ 0 & 0 & 0 & 1 \end{bmatrix}.$$

Hence, the pose of the flexible plug frame O_e with respect to the robot base frame O_b is given by

$$\boldsymbol{T}_e^b = \boldsymbol{T}_s^b \left(\boldsymbol{T}_s^e\right)^{-1} \tag{2}$$

which is the input of the inverse kinematics described in the following Section III. A.

Taking some type of electric vehicle as an example, Fig. 6 shows the information about parking lots, electric vehicles and parking errors covering majority parking situations in parking scene.

Set L_1 as the length of the parking lot, W_1 as the width of the parking lot, L_2 as the length of the electric vehicle, W_2 as the width of the electric vehicle, h_1 as the height of the DC charging port, and $\Delta\gamma$ as the angle between the central axis of the charging port and horizontal plane. In the automatic parking scene where the blockader (as shown in Fig. 1) exists, the distance between the center of the rear wheels and the rear parking line is set as L_3 after the parking is completed. This parking is called the standard parking situation. The distance between the center of the rear wheels in actual situation and that in the standard parking situation is called as the front/back parking error ΔL. The distance between the left/right central axis of the electric vehicle and that of the parking lot is called as the left/right parking error ΔW. The angle between the left/right central axis of the electric vehicle and that of the parking lot is called as the yaw parking error $\Delta\theta$.

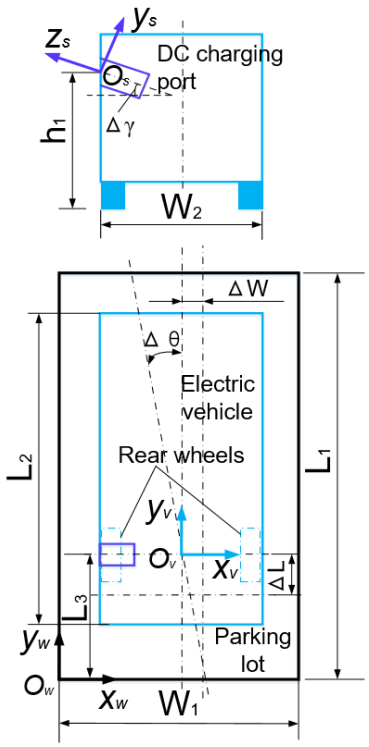

FIGURE 6. Information about parking lot, electric vehicle and parking error in parking scene.

As shown in Fig. 6, the origins of the world frame, the vehicle frame and the charging port frame are located at one corner of the parking lot, the intersection of the central axis of the rear wheels and the left/right central axis of the electric vehicle and the center of the charging port, respectively. The robot base frame (i.e., O_0 in Fig. 2) and the flexible plug frame are identical to those described in Fig. 2 and Fig. 3.

Based on this, the parameters shown in Fig. 5 can be given below. The pose of the charging port with respect to the electric vehicle can be determined by $x_{sv} = -W_2/2$, $y_{sv} = 0$, $z_{sv} = h_1$, $\alpha_{sv} = \Delta\gamma$. After the parking is completed, the pose of the electric vehicle with respect to the world frame can be determined by $x_{vw} = W_1/2 + \Delta W$, $y_{vw} = L_3 + \Delta L$, $\alpha_{vw} = \Delta\theta$. Substituting these in Eq. (2) gives the pose of the flexible plug that is a function of the parking error ΔL, ΔW and $\Delta\theta$.

2) WORKSPACE OPTIMIZATION

The basic plugging-unplugging path is shown in Fig. 7. There are four key positions involved in this path. They are starting position, pre-plugging position, plugging position, and plugging complete position. Based on this, the auto-charging process is divided into six steps. First, the plug moves to the pre-plugging position according to the pose of the charging port measured by the vision sensor. In the pre-plugging position, the plug is perfectly aligned with the

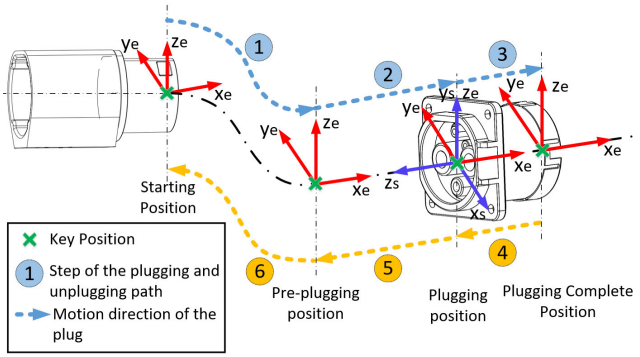

FIGURE 7. Basic plugging-unplugging path.

charging port. Second, the plug moves along the axis of the charging port to the plugging position. Third, the plug continues to move along the axis of the charging port to the plugging complete position. Fourth, the plug is unplugged to the plugging position. Then, the plug returns to pre-plugging position and starting position in sequence.

For a pose of the charging port, the pluggability of the auto-charging robot depends on whether the robot workspace contains the plugging-unplugging path. Mathematically, the plugging-unplugging workspace optimization is formulated as

$$\begin{aligned} &min \ -N_f\left(\boldsymbol{a},\boldsymbol{\alpha},\boldsymbol{x}_b^w\right) \\ &s.t. \ \boldsymbol{a}\in S_{\boldsymbol{a}}, \quad \boldsymbol{\alpha}\in S_{\boldsymbol{\alpha}}, \ \boldsymbol{x}_b^w\in S_{\boldsymbol{x}_b^w} \end{aligned} \tag{3}$$

where $\boldsymbol{a}\in\mathbb{R}_{11\times1}$, $\boldsymbol{\alpha}\in\mathbb{R}_{6\times1}$ and $\boldsymbol{x}_b^w\in\mathbb{R}_{4\times1}$ are the link lengths, the link deflection angles and the install pose of the robot, respectively. $S_{\boldsymbol{a}}$, $S_{\boldsymbol{\alpha}}$ and $S_{\boldsymbol{x}_b^w}$ is the set of possible link lengths, the link deflection angles and the install pose of robot for $\boldsymbol{a}$, $\boldsymbol{\alpha}$ and $\boldsymbol{x}_b^w$, respectively, subject to the constraints of mechanical design and actual parking scene. The objective function N_f is the total number of feasible configurations in the operational workspace for the selected combinations of $\boldsymbol{a}$, $\boldsymbol{\alpha}$ and $\boldsymbol{x}_b^w$. It can be computed by discretizing the parking error in the operational space and counting the total number of feasible configurations. For the feasible configurations, the solutions of the inverse kinematics problem are within the joint range subject to mechanical design. The inverse kinematics will be described in the following Section III. A

The total dimension of $\boldsymbol{a}$, $\boldsymbol{\alpha}$ and $\boldsymbol{x}_b^w$ is twenty-one, which makes the problem high dimensional and then computationally intensive. In fact, considering the actual mechanical design, ℓ_1, ℓ_{i1} and ℓ_{i3} $(i=2,3,4)$ of $\boldsymbol{a}$, all elements of $\boldsymbol{\alpha}$ and $\boldsymbol{x}_b^w$ can be directly determined. Only the link length ℓ_{i2} $(i=2,3,4)$ are the parameters to be optimized.

III. BASIC MODEL

A. KINEMATIC MODEL

Given $\boldsymbol{a}=[\ell_1,\ell_{21},\ell_{22},\ell_{23},\ell_{31},\ell_{32},\ell_{33},\ell_{41},\ell_{42},\ell_{43},\ell_{4e}]^T$ and $\boldsymbol{\alpha}=[\alpha_{21},\alpha_{22},\alpha_{31},\alpha_{32},\alpha_{41},\alpha_{42}]^T$, the forward kinematics of the robot can be expressed as

$$\boldsymbol{T}_e^0(\boldsymbol{q})=\boldsymbol{A}_1^0(d_1)\,\boldsymbol{A}_2^1(\theta_2)\,\boldsymbol{A}_3^2(\theta_3)\,\boldsymbol{A}_4^3(\theta_4)\,\boldsymbol{A}_e^4 \tag{4}$$

where $\boldsymbol{A}_j^i$ denotes the homogeneous transformation relating the description of a point in frame j to the description of the same point in frame i.

The inverse kinematics of the robot can be expressed as

$$\boldsymbol{q}=\boldsymbol{q}\left(\boldsymbol{T}_e^0\right) \tag{5}$$

For the 6-cable cable-driven system of CDACR, the j-th attachment point of the cable i $(i=1,2,\cdots,6)$ on link k_j is denoted by A_{ijk_j}, where k_j denotes the link number where the j-th attachment point is located. The total number of the attachment points for cable i is denoted by t_i. Therefore, cable i consists of t_i-1 cable segments, where a cable segment is defined as the section of the cable between two adjacent attachment points. For example, the j-th segment vector $(j=1,2,\cdots,t_i-1)$ is denoted by $\boldsymbol{l}_{ij}$ and the corresponding segment length is denoted by l_{ij}. The cable space for the system can be represented by the cable length vector $\boldsymbol{l}=\left[\begin{array}{cccccc}\boldsymbol{l}_1^T & \boldsymbol{l}_2^T & \boldsymbol{l}_3^T & \boldsymbol{l}_4^T & \boldsymbol{l}_5^T & \boldsymbol{l}_6^T\end{array}\right]^T\in\mathbb{R}_{30\times1}$, where $\boldsymbol{l}_1=\left[\begin{array}{ccc}l_{11} & l_{12} & l_{13}\end{array}\right]^T\in\mathbb{R}_{3\times1}$, $\boldsymbol{l}_2=\left[\begin{array}{ccc}l_{21} & l_{22} & l_{33}\end{array}\right]^T\in\mathbb{R}_{3\times1}$, $\boldsymbol{l}_3=\left[\begin{array}{ccccc}l_{31} & l_{32} & l_{33} & l_{34} & l_{35}\end{array}\right]^T\in\mathbb{R}_{5\times1}$, $\boldsymbol{l}_4=\left[\begin{array}{ccccc}l_{41} & l_{42} & l_{43} & l_{44} & l_{45}\end{array}\right]^T\in\mathbb{R}_{5\times1}$, $\boldsymbol{l}_5=\left[\begin{array}{ccccccc}l_{51} & l_{52} & l_{53} & l_{54} & l_{55} & l_{56} & l_{57}\end{array}\right]^T\in\mathbb{R}_{7\times1}$, and $\boldsymbol{l}_6=\left[\begin{array}{ccccccc}l_{61} & l_{62} & l_{63} & l_{64} & l_{65} & l_{66} & l_{67}\end{array}\right]^T\in\mathbb{R}_{7\times1}$ represent the cable segment length vectors of cable 1, cable 2, cable 3, cable 4, cable 5, and cable 6, respectively.

The j-th segment of cable i is attached from attachment point A_{ijk_j} to attachment point $A_{i(j+1)k_{j+1}}$. The corresponding cable segment vector with respect to frame O_{k_j} is defined as

$$\boldsymbol{l}_{ij}^{k_j}=\boldsymbol{R}_{k_{j+1}}^{k_j}\boldsymbol{r}_{k_{j+1},A_{i(j+1)k_{j+1}}}^{k_{j+1}}+\boldsymbol{r}_{k_j,k_{j+1}}^{k_j}-\boldsymbol{r}_{k_j,A_{ijk_j}}^{k_j} \tag{6}$$

where $\boldsymbol{r}_{k_j,A_{ijk_j}}^{k_j}$ denotes the vector from the origin of frame O_{k_j} to attachment point A_{ijk_j} with respect to frame O_{k_j}. $\boldsymbol{R}_{k_{j+1}}^{k_j}$ and $\boldsymbol{r}_{k_j,k_{j+1}}^{k_j}$ denote the rotation and translation part of the homogeneous transformation matrix $\boldsymbol{A}_{k_{j+1}}^{k_j}$ between frame O_{k_j} and frame $O_{k_{j+1}}$, respectively.

The length of the segment $\boldsymbol{l}_{ij}^{k_j}$ is denoted by $l_{ij}=\left\|\boldsymbol{l}_{ij}^{k_j}\right\|$. The length of cable i can be represented as

$$l_i=\sum_{j=1}^{t_i}l_{ij} \tag{7}$$

B. DYNAMIC MODEL

The equations of motion for 3-DOF CDSM can be expressed in the form

$$\boldsymbol{M}(\boldsymbol{q})\,\ddot{\boldsymbol{q}}+\boldsymbol{C}(\boldsymbol{q},\dot{\boldsymbol{q}})\,\dot{\boldsymbol{q}}+\boldsymbol{g}(\boldsymbol{q})=-\boldsymbol{U}^T\boldsymbol{\tau} \tag{8}$$

where $\boldsymbol{q}=\left[\begin{array}{ccc}\theta_2 & \theta_3 & \theta_4\end{array}\right]^T\in\mathbb{R}_{3\times1}$ denotes joint space for CDSM, $\boldsymbol{M}\in\mathbb{R}_{3\times3}$ denotes the inertia matrix, $\boldsymbol{C}\in\mathbb{R}_{3\times3}$ denotes the Coriolis and centrifugal terms, $\boldsymbol{g}\in\mathbb{R}_{3\times1}$ indicates the vector of gravity terms, $\boldsymbol{\tau}\in\mathbb{R}_{30\times1}$ denotes the vector of the cable segment tensions corresponding to the cable lengths vector $\boldsymbol{l}\in\mathbb{R}_{30\times1}$, $\boldsymbol{U}\in\mathbb{R}_{30\times3}$ denotes the Jacobian matrix relating cable tensions to joint moments.

Actually, matrix $\boldsymbol{U}$ is computed by $\boldsymbol{U} = \boldsymbol{VW} \in \mathbb{R}_{30\times3}$, where $\boldsymbol{V} \in \mathbb{R}_{30\times18}$ and $\boldsymbol{W} \in \mathbb{R}_{18\times3}$ denote Jacobian matrices relating cable tensions to Cartesian wrench and relating Cartesian wrench to joint moments, respectively.

The vector of cable input tensions is denoted by $\boldsymbol{\tau}_0 = \begin{bmatrix} \tau_{10} & \tau_{20} & \tau_{30} & \tau_{40} & \tau_{50} & \tau_{60} \end{bmatrix}^T \in \mathbb{R}_{6\times1}$. Assuming that the vector of cable segment tensions has linear relationship with the vector of cable input tensions, the vector of cable segment tensions can be computed by

$$\boldsymbol{\tau} = \boldsymbol{L}\boldsymbol{\tau}_0 \tag{9}$$

where $\boldsymbol{L} \in \mathbb{R}_{30\times6}$ denotes the linear relationship relating cable input tensions to cable segment tensions.

Hence, the equations of motion for CDSM can be expressed in the form

$$\boldsymbol{M}(\boldsymbol{q})\ddot{\boldsymbol{q}} + \boldsymbol{C}(\boldsymbol{q},\dot{\boldsymbol{q}})\dot{\boldsymbol{q}} + \boldsymbol{g}(\boldsymbol{q}) = \boldsymbol{H}\boldsymbol{\tau}_0 \tag{10}$$

where $\boldsymbol{H} = -\boldsymbol{U}^T\boldsymbol{L} \in \mathbb{R}_{3\times6}$ denotes Jacobian matrices relating cable input tensions to joint moments.

The magnitude of two adjacent segment tensions $T_{i,j-1}$ and $T_{i,j}$ of cable i has the following relations [30]:

$$T_{i,j} = T_{i,j-1}e^{\mu\varphi_{ij}} \tag{11}$$

where $\varphi_{ij} = \cos^{-1}\left(\bar{\boldsymbol{l}}_{i,j-1}^{k_j}\cdot\bar{\boldsymbol{l}}_{ij}^{k_j}\right)$ denotes the contact angle, μ denotes the coefficient of saturated viscous friction, $\bar{\boldsymbol{l}}_{ij}^{k_j}$ denotes the unit vector of $\boldsymbol{l}_{ij}^{k_j}$, and $\bar{\boldsymbol{l}}_{i,j-1}^{k_j}$ is computed by $\left(\boldsymbol{R}_{k_j}^{k_{j-1}}\right)^{-1}\bar{\boldsymbol{l}}_{i,j-1}^{k_{j-1}}$. Hence, the matrix $\boldsymbol{L}$ can be determined by using Eq. (11).

C. CABLE TENSION SOLVER

The equilibration of the joint torques provided by the cables tensions with the joint torques $\boldsymbol{\tau}_j \in \mathbb{R}_{3\times1}$ required by external Cartesian wrenches can be expressed as in the form

$$\boldsymbol{H}\boldsymbol{\tau}_0 = \boldsymbol{\tau}_j \tag{12}$$

Equation (12) is underdetermined since the number of cables is greater than the number of DOFs. The solution of Eq. (12) can be written as

$$\boldsymbol{\tau}_0 = \bar{\boldsymbol{\tau}}_0 + \boldsymbol{N}(\boldsymbol{H})\boldsymbol{\lambda} \tag{13}$$

where $\bar{\boldsymbol{\tau}}_0$ is the minimum norm solution of Eq. (12) derived by using the pseudo-inverse of $\boldsymbol{H}$ and is given by $\bar{\boldsymbol{\tau}}_0 = \boldsymbol{H}^T\left(\boldsymbol{H}\boldsymbol{H}^T\right)^{-1}\boldsymbol{\tau}_j$. The matrix $\boldsymbol{N}(\boldsymbol{H}) \in \mathbb{R}_{6\times3}$ is the kernel of matrix $\boldsymbol{H}$ and $\boldsymbol{\lambda} \in \mathbb{R}_{3\times1}$ is an underdetermined vector, assuming matrix $\boldsymbol{H}$ is full rank.

Considering that the tension of the cable should be kept positive and within the range of $\left[\boldsymbol{\tau}_{0,min}, \boldsymbol{\tau}_{0,max}\right]$ during the whole movement, there are the following inequalities

$$\boldsymbol{\tau}_{0,min} \le \bar{\boldsymbol{\tau}}_0 + \boldsymbol{N}(\boldsymbol{H})\boldsymbol{\lambda} \le \boldsymbol{\tau}_{0,max} \tag{14}$$

To determine the unknown vector $\boldsymbol{\lambda}$ in Eq. (13), the following linear programming is performed:

$$\begin{aligned} &min \sum_{i=1}^{3}\lambda_i \\ &s.t.\ \boldsymbol{\tau}_{0,\ min} \le \boldsymbol{\tau}_0 + \mathbf{N}(\mathbf{H})\boldsymbol{\lambda} \le \boldsymbol{\tau}_{0,max} \end{aligned} \tag{15}$$

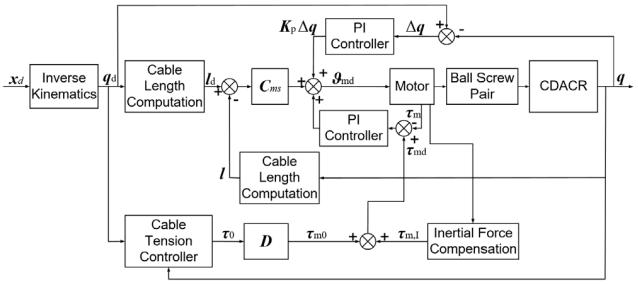

FIGURE 8. Control architecture.

In Eq. (15), the minimum sum of all elements of the unknown vector $\boldsymbol{\lambda}$ is taken as the optimization objective; Eq. (14) is taken as the constraint condition to ensure that the input tensions are within a reasonable range.

IV. CONTROLLER

A. CONTROL ARCHITECTURE

A control architecture with two controllers was designed for CDACR: a cable tension controller and a motor position controller. The cable tension controller plans the cable tensions varying with the robot configuration and ensures positive tensions. The motor position controller takes the desired cable length from the cable length computation and follows it, while introducing the close-loop feedback of joint angles and motor torque outputs. The control architecture is shown in Fig. 8.

B. CABLE TENSION CONTROLLER

For the motion equation of CDSM given in Eq. (10), the nonlinear feedback compensation is given as

$$\boldsymbol{H}\boldsymbol{\tau}_0 = \boldsymbol{M}(\boldsymbol{q})\boldsymbol{u}_q + \hat{\boldsymbol{h}}(\boldsymbol{q},\dot{\boldsymbol{q}}) \tag{16}$$

where $\hat{\boldsymbol{h}}(\boldsymbol{q},\dot{\boldsymbol{q}}) = \boldsymbol{C}(\boldsymbol{q},\dot{\boldsymbol{q}})\dot{\boldsymbol{q}} + \boldsymbol{g}(\boldsymbol{q})$. Hence, the following linear system can be got:

$$\ddot{\boldsymbol{q}} = \boldsymbol{u}_q \tag{17}$$

The choice $\boldsymbol{u}_q = \ddot{\boldsymbol{q}}_d + \boldsymbol{K}_v\left(\dot{\boldsymbol{q}}_d - \dot{\boldsymbol{q}}\right) + \boldsymbol{K}_p\left(\boldsymbol{q}_d - \boldsymbol{q}\right)$ can ensure $\boldsymbol{q}(t)$ will asymptotically track $\boldsymbol{q}_d(t)$, where $\boldsymbol{K}_v$ and $\boldsymbol{K}_p$ are positive definite and diagonal matrices. The input tensions of cables $\boldsymbol{\tau}_0$ can be solved by referring to Section III. C.

C. MOTOR POSITION CONTROLLER

The motor position controller generates the motor position command to follow the desired trajectory. The desired trajectory for the plugging-unplugging motion is firstly designed in operational space $\boldsymbol{x}_d(t)$. Then, it is transformed to the joint space $\boldsymbol{q}_d(t)$ by using the inverse kinematics described by Eq. (5). The position demand value for motors consist of cable length feedforward, closed-loop PI controller for joint angles and closed-loop PI controller for motor torque outputs.

1) Cable length feedforward: The robot motion from the current configuration $\boldsymbol{q}$ to the desired configuration $\boldsymbol{q}_d$ is realized by elongating and shortening the actuation cable with

the length difference $\Delta \boldsymbol{l}$ between current cable length $\boldsymbol{l}$ and desired cable length $\boldsymbol{l}_d$. The desired and current cable length are computed by using the desired joint angle $\boldsymbol{q}_d$ and the real-time feedback of the current joint angle $\boldsymbol{q}$, respectively. For the given cable length difference, the required change of the motor position can be given by multiplying the cable length difference by a constant $\boldsymbol{C}_{ms}$. This constant is determined by the constants of the ball screw pairs and motors. The change of the motor position is fed-forward to the motors to get reference joint angles.

2) PI Controller: The vector of motor output torques can be denoted by $\boldsymbol{\tau}_m = \left[\ \tau_{m1}\ \tau_{m2}\ \tau_{m3}\ \ \tau_{m4}\ \tau_{m5}\ \tau_{m6}\ \right]^T \in \mathbb{R}_{6\times 1}$. Set $\boldsymbol{\tau}_{md}$ as the desired motor torque outputs which consist of the inertial force compensation and the reference feedforward resulting from cable input tensions. Based on the cable input tensions, the reference feedforward part is computed by $\boldsymbol{\tau}_{m0} = \boldsymbol{D}\boldsymbol{\tau}_0$, where $\boldsymbol{D} \in \mathbb{R}_{6\times 6}$ is diagonal matrix and denotes the linear relationship relating the motor torque outputs to the cable input tensions. The diagonal elements are all equal to $i = h/(2\pi)$, where h denotes the lead of the ball screws used.

Considering the motor rotor inertia, the moment of inertia of the ball screw and the mass of slider, the inertia force compensation is necessary. The inertia force caused by these elements can be given as $\boldsymbol{\tau}_{m,I} = \boldsymbol{J}_m\ddot{\boldsymbol{\theta}}_m + \boldsymbol{J}_s\ddot{\boldsymbol{\theta}}_s + \boldsymbol{D}\boldsymbol{M}_t\ddot{\boldsymbol{x}}_t$, where $\boldsymbol{J}_m$, $\boldsymbol{J}_s$ and $\boldsymbol{M}_t$ are all diagonal matrices and denote the motor rotor inertia, the moment of inertia of the ball screw and the mass of slider, respectively. $\boldsymbol{\theta}_m$, $\boldsymbol{\theta}_s$, and $\boldsymbol{x}_t$ denote the position of motor rotor, the screw and the slider, respectively. Ignoring the elasticity between the lead screw and the motor shaft, $\boldsymbol{\theta}_s \approx \boldsymbol{\theta}_m$, $\boldsymbol{x}_t = \boldsymbol{D}\boldsymbol{\theta}_s \approx \boldsymbol{D}\boldsymbol{\theta}_m$ can be got. Based on this, the inertia force caused by these elements can be rewritten as $\boldsymbol{\tau}_{m,I} \approx (\boldsymbol{J}_m + \boldsymbol{J}_s - \boldsymbol{D}\boldsymbol{M}_t\boldsymbol{D})\ddot{\boldsymbol{\theta}}_m$. Thus, the desired motor torque outputs can be given as

$$\boldsymbol{\tau}_{md} = \boldsymbol{\tau}_{m0} + \boldsymbol{\tau}_{m,I} \tag{18}$$

To compensate the screw-ball's backhaul error, the cables' elastic deformation and the errors of cable attachment points' coordinates, two closed-loop PI controllers are applied in the joint angles $\boldsymbol{q}$ and the motor torque outputs $\boldsymbol{\tau}_m$. Here, the cable tensions are not fed back to form a closed-loop control due to the poor real-time performance of load cells. However, the motor torque outputs are used as the feedback, which allows the cable tensions to be controlled indirectly. The feedback of the joint angles and the motor torque outputs are provided by the joint encoders and the motors in real-time, respectively. Therefore, the position demand for the motors can be given by

$$\begin{aligned}\boldsymbol{\vartheta}_{md} = \boldsymbol{C}_{ms}\left(\boldsymbol{l}_d - \boldsymbol{l}\right) + \boldsymbol{K}_{pq}\left(\boldsymbol{q}_d - \boldsymbol{q}\right) + \boldsymbol{K}_{vq}\left(\dot{\boldsymbol{q}}_d - \dot{\boldsymbol{q}}\right) \\ + \boldsymbol{K}_{p\tau_m}\left(\boldsymbol{\tau}_{md} - \boldsymbol{\tau}_m\right)\end{aligned} \tag{19}$$

where $\boldsymbol{K}_{pq} \in \mathbb{R}_{6\times 3}$, $\boldsymbol{K}_{vq} \in \mathbb{R}_{6\times 3}$ and $\boldsymbol{K}_{p\tau_m} \in \mathbb{R}_{6\times 6}$ denote control parameters; $\mathbf{K}_{p\tau_m}$ are positive definite and diagonal matrix.

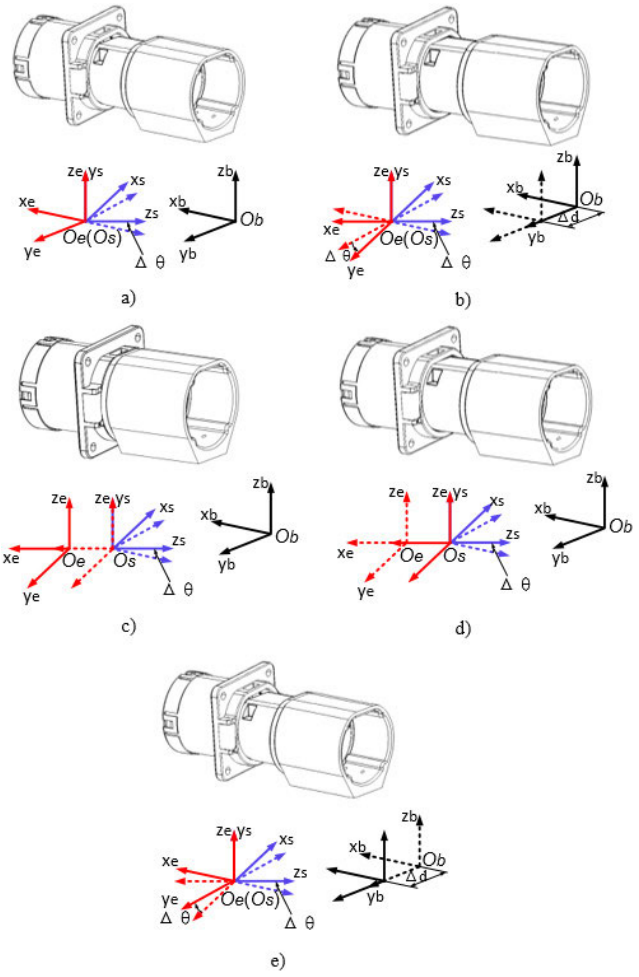

FIGURE 9. Plugging-unplugging strategy for the parking situation with yaw error. (a) the plugging position, (b) the platform moving to right, (c) the plugging complete position, (d) the plugging position, (e) the platform moving to left.

D. PLUGGING-UNPLUGGING STRATEGY

For parking situations where yaw error is present, the alignment of two frames of the charging port and the flexible plug is impossible because of the planar configuration of CDACR. In those situations, the direct plugin path shown in Fig. 7 will result in large resistance and will end in failure for plugging-unplugging. In view of this, the plugging-unplugging strategy by controlling the motion of the moving platform is proposed, as shown in Fig. 9.

Taking the parking situation with the yaw error $\Delta\theta$ being equal to 5° as an example, first, the flexible plug moves to the plugging position according to the pose of the charging port with the yaw error. At this time, the origins of the two frames coincide, but there is an angle between their orientations compared to the parking situation without yaw error, as shown in Fig. 6 (a). This angle is equal to the yaw error $\Delta\theta$. Second, the moving platform moves to the right a certain distance Δd. This results in rotational elastic deformation of the flexible plug about z_e axis. The angle above will be

TABLE 1. Joint range.

Joint	Range
d_1	± 100 mm
θ_2	$\pm 35°$
θ_3	$\pm 45°$
θ_4	$\pm 45°$

TABLE 2. parking parameters.

Parameter	Value	Parameter	Value
L_1	5000 mm	$\Delta\gamma$	30.2°
W_1	2420 mm	L_3	1000 mm
L_2	4450 mm	ΔL	[−100 mm, 100 mm]
W_2	1900 mm	ΔW	[−200 mm, 200 mm]
h_1	832.4 mm	$\Delta\theta$	[−5°, +5°]

decreased with the deformation, as shown in Fig. 6 (b). Third, the robot moves along the plugging trajectory to complete the plugging action, but this trajectory is planned under the assumption that the yaw error is equal to zero. Simultaneously, the flexible plug moves to the plugging complete position along the axis of the charging port, as shown in Fig. 6 (c). During the plugging motion, the elastic deformation will increase as the insertion depth increases. After the completement of plugging, the auto-charging robot remains stationary a certain time to simulate the charging process. Then, the manipulator moves along the unplugging trajectory to complete unplugging action. Similar to the plugging action, this trajectory is planned under the assumption that the yaw error is equal to zero. Simultaneously, the flexible plug moves to the plugging position along the axis of the charging port, as shown in Fig. 6 (d). Before the movement to the pre-plugging position, the moving platform moves the same distance as above to the left to restore the elastic deformation, as shown in Fig. 6 (e). Finally, the flexible plug returns to the pre-plugging position.

V. EXPERIMENT

A. EXPERIMENTAL DEVICE

1) LINK PARAMETERS

Considering the actual mechanical design, the link deflection angles were determined as $\boldsymbol{\alpha} = \begin{bmatrix} 0 & 35° & 35° & -35° & -35° & 0 \end{bmatrix}^T$. The partial link parameters were determined as $\ell_1 = 280$ mm, $\ell_{21} = \ell_{23} = \ell_{31} = \ell_{33} = \ell_{41} = 55$ mm. The link length ℓ_{43} were regarded as zero considering $\alpha_{42} = 0$. The length of the flexible plug was designed as $\ell_{4e} = 231.31$ mm. According to the actual installation of the flexible plug, the link length ℓ_{42} were determined as $\ell_{42} = 85.26$ mm. Hence, only link length ℓ_{22} and ℓ_{32} are to be optimized. Their ranges were set as [150 mm, 400 mm]. The joints motion range are listed in Table 1.

The detailed information of the parking parameters shown in Fig. 6 is given in Table 2.

According to the actual demand, the installation position of the robot was determined as $x_{bw} = -275mm$, $y_{bw} = L_3$, $z_{bw} = 0$, $\alpha_{bw} = 0$. Namely, the robot base is facing the charging port; the distance between the robot base and the left parking line is 275 mm; the moving direction of the moving platform is parallel to the left/right parking line, assuming the parking errors are all zeros. In Fig. 7, the distance between the pre-plugging position and plugging position is set as 20 mm. According to the actual charging port structure, the plugging depth is equal to 50 mm.

TABLE 3. Link parameters of CDACR.

Link i	ℓ_{i1}(mm)	ℓ_{i2}(mm)	ℓ_{i3}(mm)	α_{i1}(°)	α_{i2}(°)
1	280				
2	55	246	55	0	35
3	55	257	55	35	-35
4	55	85.26	0	-35	0

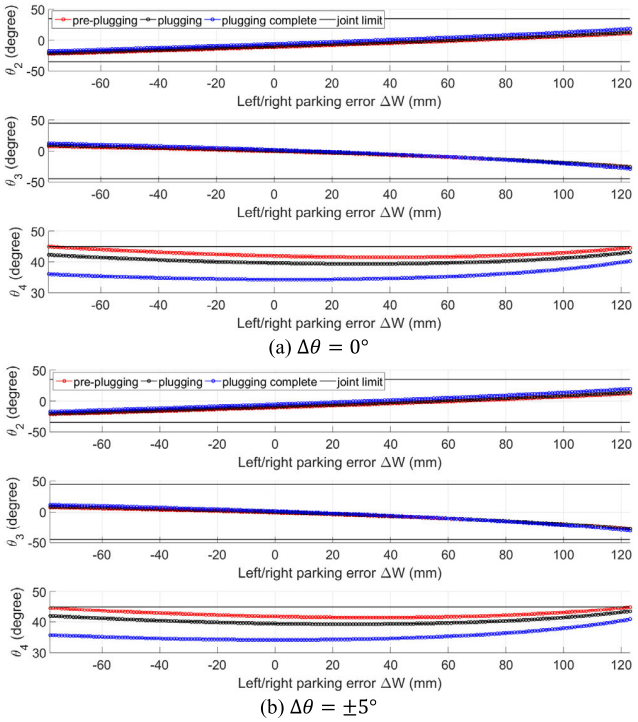

(a) $\Delta\theta = 0°$

(b) $\Delta\theta = \pm 5°$

FIGURE 10. Adaptable parking error range and the corresponding joint angles of CDACR.

The front/back parking error can be adapted by the moving platform with long enough guide. The high compliance of the flexible plug can adapt the yaw error. It is remarkable that the left/right parking error plays the most vital role in the manipulator design. The left/right parking error shown in Table 1 was discretized into 401 error points at interval of 1mm. Each error point corresponds to one charging port pose computed by using Eq. (2). By using the optimization algorithm described in Eq. (6), the optimized link lengths are $\ell_{22} = 246$mm and $\ell_{32} = 257$mm. The link parameters of CDACR are shown in Table 3.

The adaptable parking error range and the corresponding joint angles of CDACR are shown in Fig. 10.

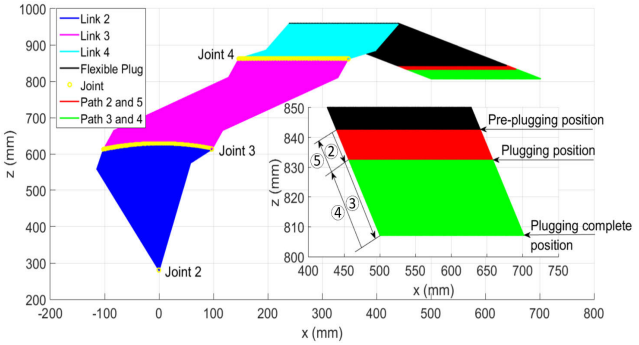

FIGURE 11. Plots of CDACR and the corresponding poses of charging port.

According to Fig. 10, the plugging-unplugging workspace is $\Delta W \in [-78\text{ mm}, 123\text{ mm}]$. The corresponding joint angles are all in the joint motion range shown in Table 1.

The plots of CDACR and the corresponding poses of the charging port are shown in Fig. 11. When the left/right parking error ΔW is equal to -78 mm and 123 mm and the front/back parking error ΔL is equal to zero, the corresponding coordinates of the charging port with respect to the robot base frame O_b are $x_{bs} = (W_1 - W_2)/2 + \Delta W - x_{bw} = 462$ mm, $y_{bs} = 0$, $z_{bs} = h_1 = 832.4$ mm and $x_{bs} = 658$ mm, $y_{bs} = 0$, $z_{bs} = 832.4$ mm, respectively. These positions of the charging ports are the pluggable point closest and farthest to the robot base, respectively, assuming the height of charging port is 832.4 mm.

Considering the translational motion of the moving platform, the pluggable workspace is a rectangular plane that is at the height of the charging port from the ground. Its length and width are the moving range of the platform and the distance between the closest and farthest pluggable points, respectively.

2) CABLE ROUTING

The detailed information of the cable routing path of CDACR is given in Table 4. The cable routing information includes cable i, the j-th attachment point of the cable i, body number k_j where the j-th attachment point is located, attachment point A_{ijk_j} and the vector from origin of frame O_{k_j} to attachment point A_{ijk_j} with respect frame O_{k_j}. The vectors $\boldsymbol{r}^1_{1,A_{111}}$, $\boldsymbol{r}^1_{1,A_{121}}$, $\boldsymbol{r}^1_{1,A_{211}}$, $\boldsymbol{r}^1_{1,A_{221}}$, $\boldsymbol{r}^1_{1,A_{311}}$, $\boldsymbol{r}^1_{1,A_{321}}$, $\boldsymbol{r}^1_{1,A_{411}}$, $\boldsymbol{r}^1_{1,A_{421}}$, $\boldsymbol{r}^1_{1,A_{511}}$, $\boldsymbol{r}^1_{1,A_{521}}$, $\boldsymbol{r}^1_{1,A_{611}}$, and $\boldsymbol{r}^1_{1,A_{621}}$ are not necessary for the prosed controller. Hence, their values are not listed. According to Table 4, the routings of the cables numbered 1, 3 and 5 are symmetrical with those of cables numbered 2, 4 and 6, respectively. The y coordinates of the attachment points of the same cable are identical to eliminate the friction between the cables and the side of the pulleys.

3) DYNAMIC PARAMETERS

The dynamic parameters, including relative position relationship between adjacent link frames $\boldsymbol{r}^k_{k-1,k}$, link center of mass $\boldsymbol{r}^k_{k,C_k}$, link mass m_k, and y component of inertia tensor relative to the centre of mass of link k with respect to current frame $I^k_{k,yy}$ of CDSM are given in Table 5.

TABLE 4. Cable distribution of CDACR.

i	j	k_j	A_{ijk_j}	$\boldsymbol{r}^{k_j}_{k_j,A_{ijk_j}}$(mm)
1	1	1	A_{111}	$\boldsymbol{r}^1_{1,A_{111}}$
	2	1	A_{121}	$\boldsymbol{r}^1_{1,A_{121}}$
	3	1	A_{131}	$\boldsymbol{r}^1_{1,A_{131}}$(-135, 4, -75)
	4	2	A_{142}	$\boldsymbol{r}^2_{2,A_{142}}$(89.4932, 4.0000, -292.6467)
2	1	1	A_{211}	$\boldsymbol{r}^1_{1,A_{211}}$
	2	1	A_{221}	$\boldsymbol{r}^1_{1,A_{221}}$
	3	1	A_{231}	$\boldsymbol{r}^1_{1,A_{231}}$(135, 4, -75)
	4	2	A_{242}	$\boldsymbol{r}^2_{2,A_{242}}$(192.7064, 4.0000, -220.3761)
3	1	1	A_{311}	$\boldsymbol{r}^1_{1,A_{311}}$
	2	1	A_{321}	$\boldsymbol{r}^1_{1,A_{321}}$
	3	1	A_{331}	$\boldsymbol{r}^1_{1,A_{331}}$(-95, 24.5, -75)
	4	2	A_{342}	$\boldsymbol{r}^2_{2,A_{342}}$(83.1839, 24.5000, -283.6360)
	5	2	A_{352}	$\boldsymbol{r}^2_{2,A_{352}}$(-63, 24.5, -34)
	6	3	A_{363}	$\boldsymbol{r}^3_{3,A_{363}}$(-210.4091, 24.5000, -265.5221)
4	1	1	A_{411}	$\boldsymbol{r}^1_{1,A_{411}}$
	2	1	A_{421}	$\boldsymbol{r}^1_{1,A_{421}}$
	3	1	A_{431}	$\boldsymbol{r}^1_{1,A_{431}}$(95, 24.5, -75)
	4	2	A_{442}	$\boldsymbol{r}^2_{2,A_{442}}$(186.3970, 24.5000, -211.3654)
	5	2	A_{452}	$\boldsymbol{r}^2_{2,A_{452}}$(63, 24.5, -34)
	6	3	A_{463}	$\boldsymbol{r}^3_{3,A_{463}}$(-84.4091, 24.5000, -265.5221)
5	1	1	A_{511}	$\boldsymbol{r}^1_{1,A_{511}}$
	2	1	A_{521}	$\boldsymbol{r}^1_{1,A_{521}}$
	3	1	A_{531}	$\boldsymbol{r}^1_{1,A_{531}}$(-55, -16.5, -75)
	4	2	A_{542}	$\boldsymbol{r}^2_{2,A_{542}}$(83.1839, -16.5000, -283.6360)
	5	2	A_{552}	$\boldsymbol{r}^2_{2,A_{552}}$(-63, -16.5, -34)
	6	3	A_{563}	$\boldsymbol{r}^3_{3,A_{563}}$(-210.4091, -16.5000, -254.5221)
	7	3	A_{573}	$\boldsymbol{r}^3_{3,A_{573}}$(-63, -16.5, -34)
	8	4	A_{584}	$\boldsymbol{r}^4_{4,A_{584}}$(-54.0640, -16.5000, -55.7440)
6	1	1	A_{611}	$\boldsymbol{r}^1_{1,A_{611}}$
	2	1	A_{621}	$\boldsymbol{r}^1_{1,A_{621}}$
	3	1	A_{631}	$\boldsymbol{r}^1_{1,A_{631}}$(55, -16.5, -75)
	4	2	A_{642}	$\boldsymbol{r}^2_{2,A_{642}}$(186.3970, -16.5000, -211.3654)
	5	2	A_{652}	$\boldsymbol{r}^2_{2,A_{652}}$(63, -16.5, -34)
	6	3	A_{663}	$\boldsymbol{r}^3_{3,A_{663}}$(-84.4091, -16.5000, -254.5221)
	7	3	A_{673}	$\boldsymbol{r}^3_{3,A_{673}}$(63, -16.5, -34)
	8	4	A_{684}	$\boldsymbol{r}^4_{4,A_{684}}$(54.0640, -16.5000, -131.4560)

TABLE 5. Dynamic parameters.

k	$\boldsymbol{r}^k_{k-1,k}$ (mm)	$\boldsymbol{r}^k_{k,C_k}$ (mm)	m_k (kg)	$I^k_{k,yy}$ (kg · m^2)
2	$\boldsymbol{r}^2_{1,2}$(-172.6465, 0, 301.5648)	$\boldsymbol{r}^2_{2,C_2}$(69.546, 0, -151.56)	5.0581	0.067485
3	$\boldsymbol{r}^3_{2,3}$(147.4091, 0, 320.5221)	$\boldsymbol{r}^3_{3,C_3}$(-73.136, 1.0443, -152.26)	4.7451	0.074783
4	$\boldsymbol{r}^4_{3,4}$(31.5467, 0, 130.3134)	$\boldsymbol{r}^4_{4,C_4}$(45.647, 1.2137, -56.243)	1.2456	0.017632

4) EXPERIMENTAL DEVICE

The plugging-unplugging experiment system is designed. The photograph of the system is shown in Fig. 12. Due to the

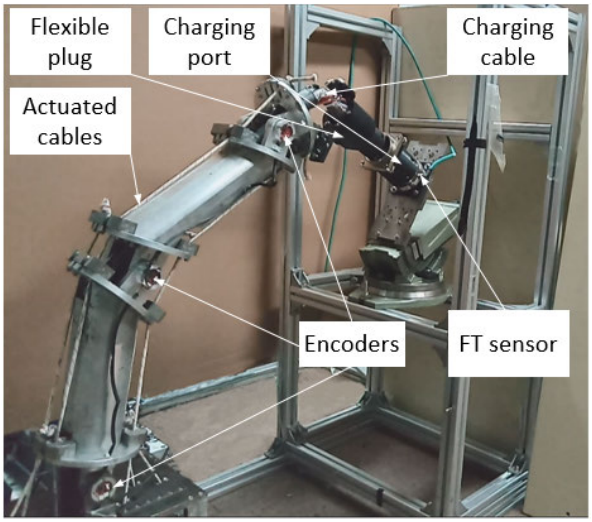

FIGURE 12. Protype of the plugging-unplugging experiment system.

limited lab environment, the electric vehicle was simulated by the charging port fixed at a holder.

B. EXPERIMENT SETUP

The experiment was designed as a plugging-unplugging task for the flexible plug and the DC charging port to see if CDACR can successfully realize automatic charging.

Based on the given pose of the charging port measured by vision sensor, the goal of this experiment is to plan the motion between pre-plugging position and plugging complete position, and then realize the plugging and unplugging action, by applying the proposed controller and the plugging-unplugging strategy.

Due to the enough guide of the moving platform, the front/back parking error $\Delta L \in [-100\text{mm}, 100\text{mm}]$ can be adapted. Without losing generality, the front/back parking error was set as zero. To prove that CDACR can complete the charging task under arbitrary positions and orientations of the charging ports, the experiments were carried out under multiple combinations of the left/right and yaw errors. The corresponding poses of the flexible plug frame with respect to the robot base frame $\boldsymbol{x}_e^b$ were computed by using Eq. (2), as shown in Table 6.

The time history of the auto-charging process is shown in Table 7. Because of the unmodeled stiffness of the flexible plug and the cable system, according to the actual debugging experience, the left/right moving distance Δd was set as 20 mm when the yaw error is equal to $\pm 5°$.

The control parameters used during this experiment were determined in the following. For the cable tension solver, the minimum cable tension vector was set as $\boldsymbol{\tau}_{0,min} = [0, 0, 0, 0, 0, 0]^T$ N, the maximum cable tension vector was set as $\boldsymbol{\tau}_{0,max} = [3000, 3000, 3000, 3000, 3000, 3000]^T$ N. For the cable tension controller, its parameters were set as $\boldsymbol{K}_p = \text{diag}\,(1000, 1000, 1000)$, $\boldsymbol{K}_v = \text{diag}\,(0, 0, 0)$, $\mu = 0.2$. For motor position controller, its parameters were set as $\boldsymbol{C}_{ms} = \text{diag}\,(22000, 22000, 22000, 22000, 22000, 22000)$, $h = 4\text{mm}$, $\boldsymbol{J}_m = 96\text{g}\cdot\text{cm}^2$, $\boldsymbol{J}_s = 68\text{g}\cdot\text{cm}^2$, $\boldsymbol{M}_t = 386$ g, $\boldsymbol{K}_{pq} = [1000, 0, 0; 1000, 0, 0; 0, 2000, 0; 0, 2000, 0; 0, 0, 3000; 0, 0, 3000;]$, $\boldsymbol{K}_{vq} = \boldsymbol{0}_{6\times 3}$, and $\boldsymbol{K}_{p\tau_m} = \text{diag}\,(20, 20, 20, 20, 10, 10)$.

TABLE 6. Experiment setup.

No	ΔW (mm)	$\Delta\theta$ (°)	$\boldsymbol{x}_e^b$ (x, y, z, R, P, Y) (plugging position)
1		-5	(460.6, 81.9, 832.4, 30.2, 0, -5)
2	-78	0	(457.0, 0, 832.4, 30.2, 0, 0)
3		5	(468.6, -81.9, 832.4, 30.2, 0, 5)
4		-5	(468.6, 81.9, 832.4, 30.2, 0, -5)
5	-70	0	(465.0, 0, 832.4, 30.2, 0, 0)
6		5	(468.6, -81.9, 832.4, 30.2, 0, 5)
7		-5	(498.6, 81.9, 832.4, 30.2, 0, -5)
8	-40	0	(495.0, 0, 832.4, 30.2, 0, 0)
9		5	(498.6, -81.9, 832.4, 30.2, 0, 5)
10		-5	(528.6, 81.9, 832.4, 30.2, 0, -5)
11	-10	0	(525.0, 0, 832.4, 30.2, 0, 0)
12		5	(528.6, -81.9, 832.4, 30.2, 0, 5)
13		-5	(538.6, 81.9, 832.4, 30.2, 0, -5)
14	0	0	(535.0, 0, 832.4, 30.2, 0, 0)
15		5	(538.6, -81.9, 832.4, 30.2, 0, 5)
16		-5	(558.6, 81.9, 832.4, 30.2, 0, -5)
17	20	0	(555.0, 0, 832.358, 30.2, 0, 0)
18		5	(558.6, -81.9, 832.4, 30.2, 0, 5)
19		-5	(588.6, 81.9, 832.4, 30.2, 0, -5)
20	50	0	(585.0, 0, 832.4, 30.2, 0, 0)
21		5	(588.6, -81.9, 832.4, 30.2, 0, 5)
22		-5	(618.6, 81.9, 832.4, 30.2, 0, -5)
23	80	0	(615.0, 0, 832.4, 30.2, 0, 0)
24		5	(618.6, -81.9, 832.4, 30.2, 0, 5)
25		-5	(648.6, 81.9, 832.4, 30.2, 0, -5)
26	110	0	(645.0, 0, 832.358, 30.2, 0, 0)
27		5	(648.6, -81.9, 832.4, 30.2, 0, 5)
28		-5	(661.6, 81.9, 832.4, 30.2, 0, -5)
29	123	0	(658.0, 0, 832.4, 30.2, 0, 0)
30		5	(661.6, -81.9, 832.4, 30.2, 0, 5)

TABLE 7. Time history of the auto-charging process.

$\Delta\theta$ (°)	Time (s)	Step of Fig. 7
0	0~2	②
	2~6	③
	6~14	Charging
	14~18	④
	18~20	⑤
±5	0~2	②
	2~4	Left 20 mm (−5°) or right 20 mm (5°)
	4~8	③
	8~12	Charging
	12~16	④
	16~18	Right 20 mm (−5°) or left 20 mm (5°)
	18~20	⑤

C. EXPERIMENT RESULTS

The experiment results were used to show the controller performance for CDACR and the device performance on automatic charging for electric vehicles.

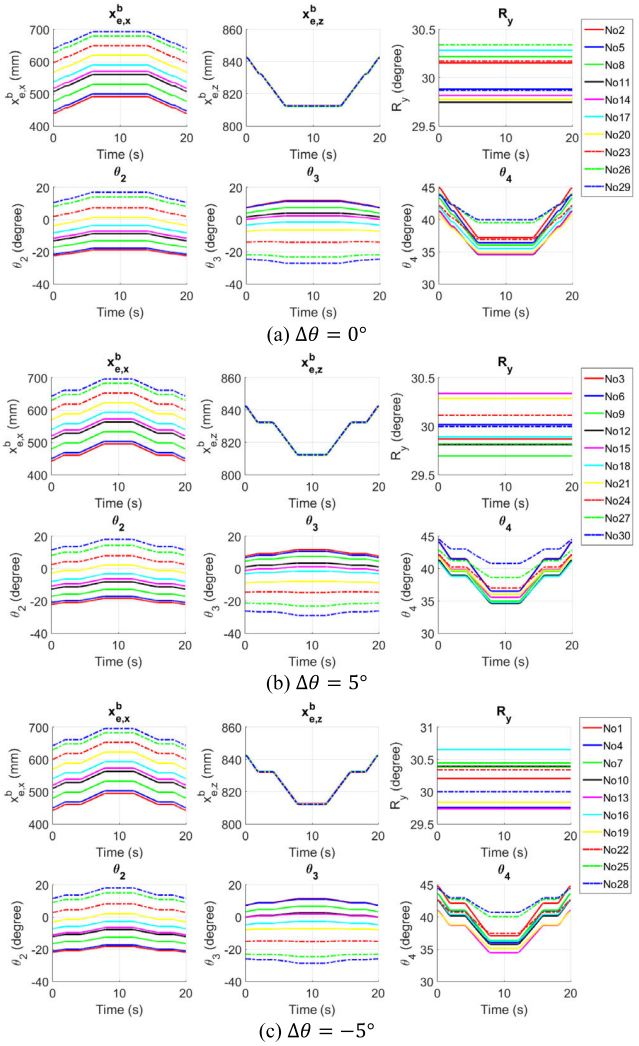

FIGURE 13. Plots of the trajectory according to the vision sensor measurements.

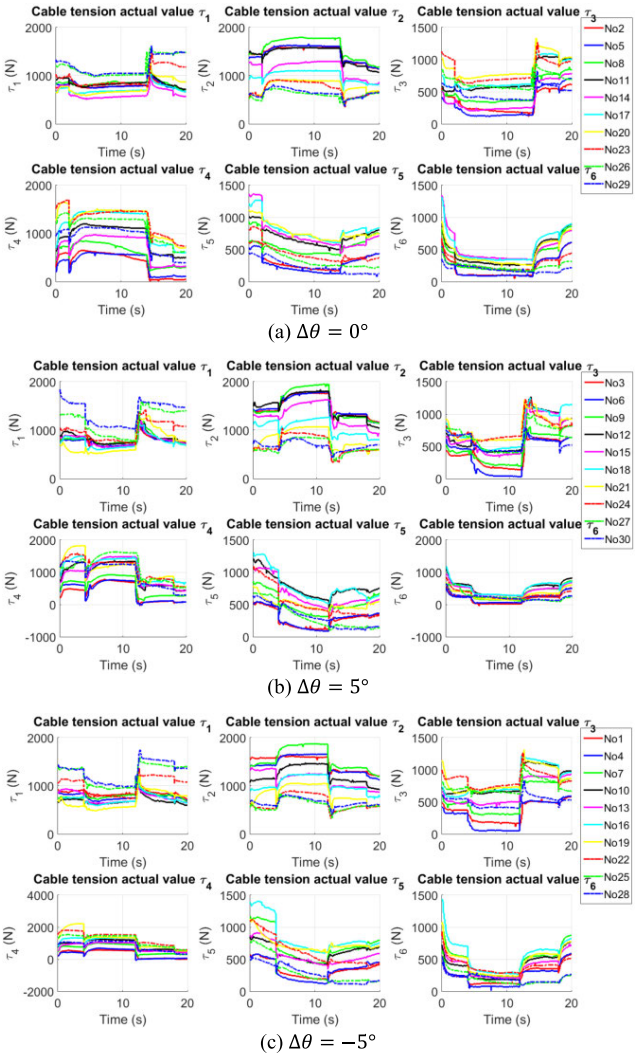

FIGURE 14. Experiment results of the cable tensions.

1) DESIRED TRAJECTORY BASDE ON VISION SENSOR MEASUREMENTS

According to Table 6, the holder was fixed at different poses to simulate the different parking situations. The poses of charging port were measured by the vision sensor. The positioning error of the vision sensor is 0.25mm for position and 0.5° for orientation. Based on the measured charging port pose, the trajectory between the pre-plugging position and the plugging complete position is planned.

For the position of the flexible plug, the trapezoidal velocity profiles for the path length is applied, where the path length denotes the length from initial point to any point in the planned path. For the orientation of the flexible plug, the desired trajectory is required that the R_x, R_y, and R_z angles keep constant with time during the whole robot maneuver. The planned trajectories are shown in Fig. 13.

2) CABLE TENSION CONTROLLER

The cable tension controller showed good performance on keeping positive cable tension during the experiment. The cable tensions of these thirty setups described in Table 6 are shown in Fig. 14. However, the tensions of cable 4 (in No3, No4, No6) and cable 6 (in No3) were negative at about 12s and 5s, respectively. This was mainly due to the delay of the flexible plug's response to the robot motion at unplugging and plugging moment, respectively.

The tensions of cable 3 (in No2, No5, No3, No6, No1, No4) and cable 6 (in No2, No5, No3, No6, No1, No4) were fairly low during the plugging process. The tensions of cable 4 (in No2, No5, No3, No6, No1, No4) and cable 5 (in No26, No29, No27, No30, No25, No28) were fairly low during the unplugging process. This was because the joint angles are approach to the limit value shown in Table 1. During the entire auto-charging process, the error accumulation in these experiments was much larger than that in other experiments because of the emerged large joint angles.

3) MOTOR POSITION CONTROLLER

The trajectory tracking errors are shown in Fig. 15. The y coordinate changed a certain distance given by Table 7 with

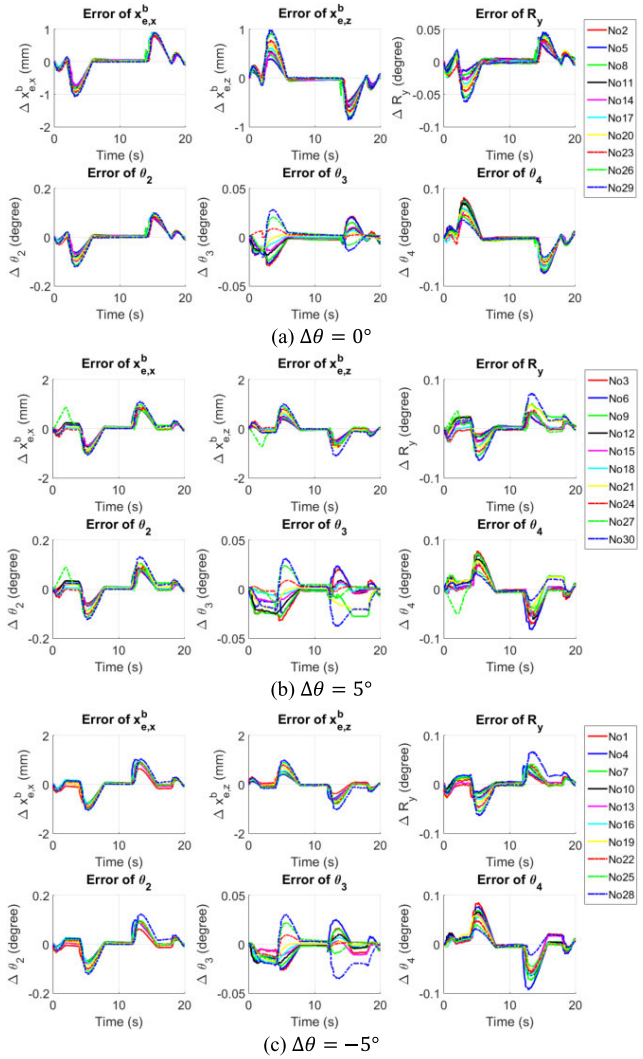

(a) $\Delta\theta = 0°$

(b) $\Delta\theta = 5°$

(c) $\Delta\theta = -5°$

FIGURE 15. Experiment results of the positioning, orientation errors and the corresponding joint angle errors.

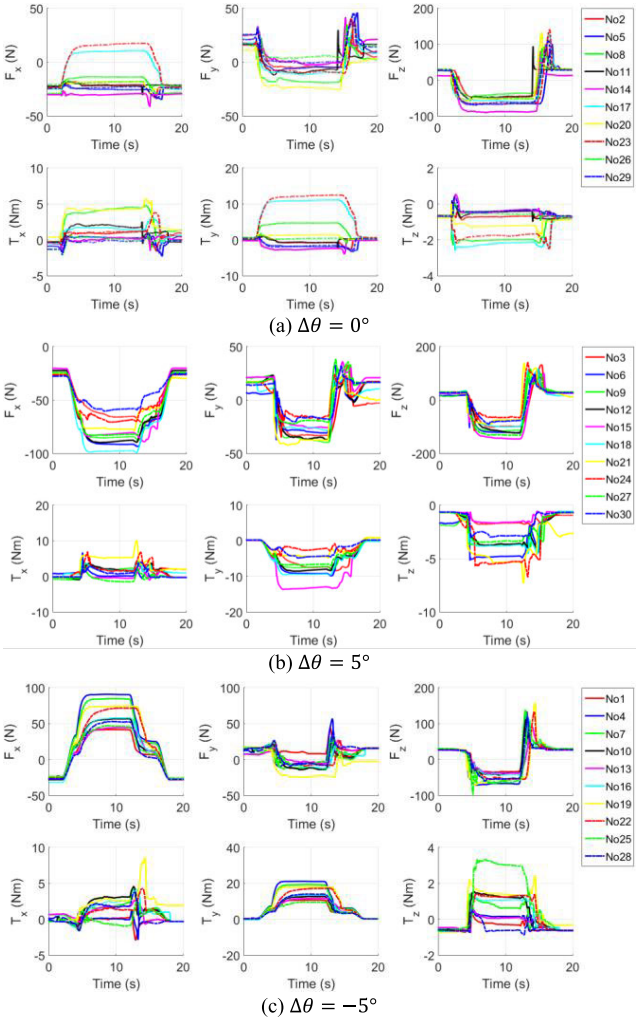

(a) $\Delta\theta = 0°$

(b) $\Delta\theta = 5°$

(c) $\Delta\theta = -5°$

FIGURE 16. Experiment results of the interaction forces/torques.

uniform speed. As shown in Fig. 15, the trajectory tracking errors of the operational space were all in ± 2 mm for position and $\pm 0.1°$ for orientation. The elastic deformation caused by these tracking errors was within the elastic limit of the elastic element. In addition, the tracking errors during plugging-unplugging process (step 3 and 4 described in Fig. 7) were higher than the tracking errors during other process. Simultaneously, these errors kept positive or negative all the time. This showed that the plugging and unplugging resistance caused large delay on the flexible plug's response to robot motion.

To ensure successful plugging and unplugging action, the positioning and orientation accuracy should be in the range of ± 1 mm and $\pm 0.5°$. Obviously, the positioning and orientation errors shown in Fig. 15 satisfied this requirement.

The plugging and unplugging interaction forces/torques are shown in Fig. 16. The maximum forces/torques during the plugging-unplugging process are shown in Table 8, 9 and 10. The following observations were obtained from these experimental results.

1) During the plugging process, the magnitudes of the forces/torques increased gradually in one direction, but they increased instantaneous in the reverse direction at the unplug moment (at 14s for $\Delta\theta = 0°$ and at 12s for $\Delta\theta = \pm 5°$). This was mainly due to the existence of transient shock.
2) The plugging and unplugging force required in the standard is not higher than 140 N. All value in Table 8 and 9 were less than this threshold. Only F_z value of No19 during unplugging were out of this requirement. Thus, this experiment was not successful.
3) The F_x value of the situation with $\Delta\theta = \pm 5°$ were larger than that of the situation without yaw error. This was mainly due to the right/left movement of the moving platform. Simultaneously, these movement had little effect on the F_y value, which can be illustrated by Table 9.

TABLE 8. Maximum force/torque Fx.

No	③ (N)	④ (N)	No	③ (N)	④ (N)	No	③ (N)	④ (N)
1	41.4	41.3	2	24.0	33.5	3	63.8	71.3
4	90.8	90.4	5	25.0	34.8	6	91.2	93.4
7	84.5	84.3	8	30.1	29.5	9	85.3	88.0
10	55.5	56.9	11	22.3	30.6	12	89.8	89.5
13	42.6	44.4	14	31.6	41.2	15	84.1	88.9
16	56.4	58.2	17	24.2	24.4	18	98.6	99.2
19	74.0	74.5	20	24.4	30.1	21	76.8	78.7
22	68.1	71.8	23	22.5	22.1	24	69.0	69.9
25	45.9	45.4	26	21.0	26.5	27	83.0	82.7
28	50.9	52.5	29	24.6	34.2	30	60.2	59.1

TABLE 9. Maximum force/torque Fy.

No	③ (N)	④ (N)	No	③ (N)	④ (N)	No	③ (N)	④ (N)
1	14.6	44.7	2	17.1	40.3	3	33.5	33.2
4	21.1	56.7	5	22.2	46.2	6	37.5	32.7
7	17.4	30.9	8	18.2	23.1	9	36.0	39.7
10	22.9	22.2	11	17.2	29.9	12	35.0	36.9
13	16.4	26.9	14	33.2	41.9	15	24.0	35.9
16	25.4	19.2	17	18.8	35.8	18	26.9	28.7
19	24.0	24.2	20	24.4	25.6	21	42.1	38.2
22	24.1	27.1	23	19.8	36.6	24	35.1	24.1
25	25.9	27.9	26	32.0	35.0	27	22.2	38.2
28	26.7	40.5	29	32.0	46.0	30	20.2	32.1

TABLE 10. Maximum force/torque Fz.

No	③ (N)	④ (N)	No	③ (N)	④ (N)	No	③ (N)	④ (N)
1	35.5	80.8	2	48.7	99.0	3	101.6	132.4
4	71.4	133.5	5	69.7	101.2	6	120.0	123.1
7	67.6	137.9	8	56.5	92.3	9	113.7	117.2
10	41.8	111.4	11	53.5	94.5	12	112.5	121.9
13	37.4	91.8	14	89.0	87.4	15	137.2	139.8
16	42.0	111.1	17	56.0	127.8	18	97.0	118.2
19	70.4	**157.7**	20	57.1	133.7	21	89.6	139.1
22	53.8	133.9	23	66.4	139.2	24	116.2	138.5
25	97.9	107.8	26	47.9	88.3	27	130.9	131.5
28	59.9	119.9	29	66.7	110.3	30	89.4	96.4

4) The F_z value of the situation with yaw error (Fig. 17(b) and (c)) and without yaw error (Fig. 17 (a)) had no significant difference in maximum force. This showed that the plugging-unplugging strategy illustrated in Section IV. D worked effectively.

The photographs of the plugging and unplugging motion of No14 and No15 are shown in Fig. 17.

From these results, it can be seen that the cable tension controller is able to keep the cable tensions positive. The moving distance must be chosen carefully as the appropriate value can apparently decrease F_z value, otherwise it may lead to a failed plugging or unplugging. In the above experiments, the selected moving distance (shown in Table 7) achieved good plugging-unplugging performance for current yaw error. However, more investigations should be carried out when CDACR is used with real electric vehicles.

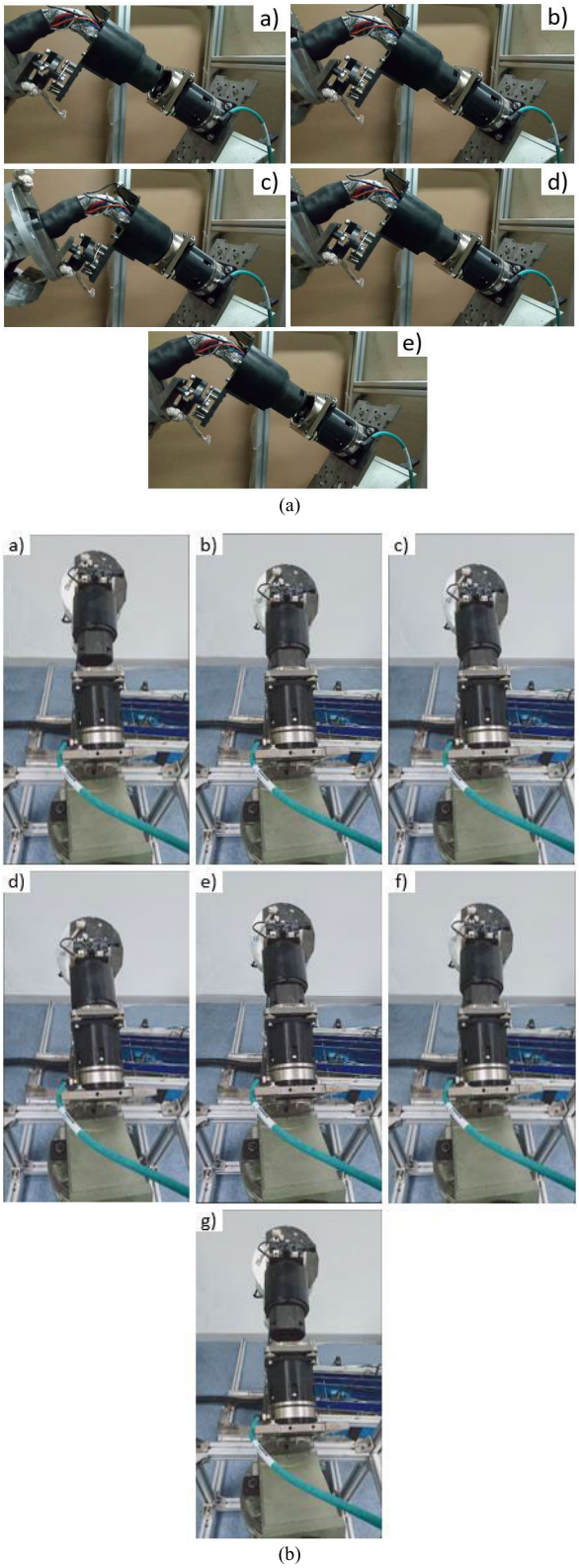

FIGURE 17. Photographs of the plugging and unplugging motion of N14 (a) and No15 (b).

VI. CONCLUSION AND FUTURE WORK

This paper presented the design of CDACR—a cable-driven auto-charging robot for electric vehicles. By applying the

cable-driven approach, there are the following remarkably advantages: 1) High compliance because of the flexibility of flexible plug and cables. 2) High ingress protection (IP) level because of the rear motors. 3) Low economic cost due to the absence of expensive reducer. 4) Lighter weight than traditional articulated manipulator. These merits provide better adaptability for the complex auto-charging situations.

CDACR possesses only 4 DOFs, but the combination of CDACR and the flexible plug is enough for a real charging mission. Compare to the existing robot-based auto-charging devices, this design is simpler and more effective for actual auto-charging. In addition, the design of deflected link reduces the joint limits of CDSM effectively in the auto-charging process. The link lengths, link deflection angles and install pose of robot were optimized to maximize the plugging-unplugging workspace, which improves CDACR's adaptability for the parking errors directly.

Preliminary experiments were carried out under different parking situations to verify the capabilities of the system. Statistical results showed that by using the proposed controller and the plugging-unplugging strategy, the plugging-unplugging interaction forces could satisfy the requirement in the standard, while all cable tensions being keep positive. CDACR was able to successfully realize the connection of the plug and the charging port in the plugging-unplugging workspace. This proved that the use of cable-driven robots in auto-charging for electric vehicles is feasible and effective.

Further studies will focus on improving its practicability. First, the stiffness control of CDACR will be carried out to reduce the possibility of damage to electric vehicles. Based on this, the proposed plugging-unplugging strategy will be further developed. Second, reducing the number of actuation cables, for example, five, four, or three cables (under-constrained robot) and developing corresponding controllers will be carried out. Third, self-calibration for the cable attachment points will be developed to improve the model of CDACR.

REFERENCES

[1] M. Kane. (Aug. 13, 2017). *Volkswagen Turns To Kuka For Robots For Autonomous Electric Cars*. Accessed: Jul. 29, 2019. [Online]. Available: https://insideevs.com/news/333887/volkswagen-turns-to-kuka-for-robots-for-autonomous-electric-cars/

[2] J. Miseikis, M. Ruther, B. Walzel, and M. Hirz, "3D vision guided robotic charging station for electric and plug-in hybrid vehicles," Mar. 2017, *arXiv:1703.05381*. [Online]. Available: https://arxiv.org/abs/1703.05381

[3] N. Zart. (Sep. 9, 2014). *PowerHydrant Charges Tesla Using Robotic Arm*. Accessed: Jul. 29, 2019. [Online]. Available: https://www.teslarati.com/powerhydrant-charges-tesla-robotic-arm/

[4] KoreaTechDesk. (Nov. 22, 2018). *EVAR: Samsung Electronics' Spinoff Brings an Autonomous Robotic Charger for Electric Vehicles*. Accessed: Jul. 29, 2019. [Online]. Available: https://koreatechdesk.com/evar-samsung-electronics-spinoff-brings-an-autonomous-robotic-charger-for-electric-vehicles/

[5] R. Bishop. (Aug. 6, 2015). *A Robotic Snake Arm is Here to Charge Your Tesla*. Accessed: Jul. 29, 2019. [Online]. Available: https://www.popularmechanics.com/cars/hybrid-electric/a16773/tesla-robotic-charging-arm/

[6] B. Walzel, C. Sturm, J. Fabian, and M. Hirz, "Automated robot-based charging system for electric vehicles," in *Proc. 16. Int. Stuttgarter Symp.*, Apr. 2016, pp. 937–949.

[7] J. T. Bryson, "The optimal design of cable-driven robots," Ph.D. dissertation, Dept. Mech. Eng., Univ. Delaware, Newark, DE, USA, 2016.

[8] Y. Mao and S. K. Agrawal, "Design of a cable-driven arm exoskeleton (CAREX) for neural rehabilitation," *IEEE Trans. Robot.*, vol. 28, no. 4, pp. 922–931, Aug. 2012.

[9] J. T. Bryson, X. Jin, and S. K. Agrawal, "Optimal design of cable-driven manipulators using particle swarm optimization," *J. Mech. Robot.*, vol. 8, no. 4, pp. 1–8, Aug. 2016.

[10] X. Cui, W. Chen, X. Jin, and S. K. Agrawal, "Design of a 7-DOF cable-driven arm exoskeleton (CAREX-7) and a controller for dexterous motion training or assistance," *IEEE/ASME Trans. Mechatronics*, vol. 22, no. 1, pp. 161–172, Feb. 2017.

[11] S. K. Agrawal, V. N. Dubey, and J. J. Gangloff, "Design and optimization of a cable driven upper arm exoskeleton," *J. Med. Devices*, vol. 3, no. 3, pp. 1–8, Jun. 2009.

[12] J. Bolboli, M. A. Khosravi, and F. Abdollahi, "Stiffness feasible workspace of cable-driven parallel robots with application to optimal design of a planar cable robot," *Robot. Auto. Syst.*, vol. 114, pp. 19–28, Apr. 2019.

[13] H. Hong, J. Ali, and L. Ren, "A review on topological architecture and design methods of cable-driven mechanism," *Adv. Mech. Eng.*, vol. 10, no. 5, May 2018, Art. no. 168781401877418.

[14] M. A. Laribi, G. Carbone, and S. Zeghloul, "Optimal design of cable driven robot for rehabilitation with prescribed workspace," in *Proc. 6th Int. Workshop MESROB*, Cassino, Italy, vol. 65, 2019, pp. 273–282.

[15] H. Ren, Q. Li, B. Liu, and Z. Dou, "Design and optimization of an elastic linkage quadruped robot based on workspace and tracking error," *Proc. Inst. Mech. Eng., C, J. Mech. Eng. Sci.*, vol. 232, no. 22, pp. 4152–4166, Nov. 2018.

[16] B. Zhang, W.-W. Shang, S. Cong, and Y. Liu, "Size optimization of the moving platform for cable-driven parallel manipulators based on stiffness characteristics," *Proc. Inst. Mech. Eng., C, J. Mech. Eng. Sci.*, vol. 232, no. 11, pp. 2057–2066, Jun. 2018.

[17] L. Gagliardini, S. Caro, M. Gouttefarde, P. Wenger, and A. Girin, "Optimal design of cable-driven parallel robots for large industrial structures," in *Proc. IEEE Int. Conf. Robot. Autom. (ICRA)*, May 2014, pp. 5744–5749.

[18] A. Nasr and S. A. A. Moosavian, "Multi-criteria design of 6-DoF fully-constrained cable driven redundant parallel manipulator," in *Proc. 3rd RSI Int. Conf. Robot. Mechatronics (ICROM)*, Tehran, Iran, Oct. 2015, pp. 1–6.

[19] H. Lamine, S. Bennour, and L. Romdhane, "Design of cable-driven parallel manipulators for a specific workspace using interval analysis," *Adv. Robot.*, vol. 30, no. 9, pp. 585–594, May 2016.

[20] X. Q. Tang and R. Yao, "Dimensional design on the six-cable driven parallel manipulator of FAST," *J. Mech. Des.*, vol. 133, no. 11, pp. 1–12, Nov. 2011.

[21] D. Lau, D. Oetomo, and S. K. Halgamuge, "Generalized modeling of multilink cable-driven manipulators with arbitrary routing using the cable-routing matrix," *IEEE Trans. Robot.*, vol. 29, no. 5, pp. 1102–1113, Oct. 2013.

[22] D. Lau, D. Oetomo, and S. K. Halgamuge, "Inverse dynamics of multilink cable-driven manipulators with the consideration of joint interaction forces and moments," *IEEE Trans. Robot.*, vol. 31, no. 2, pp. 479–488, Apr. 2015.

[23] S. Rezazadeh and S. Behzadipour, "Workspace analysis of multibody cable-driven mechanisms," *J. Mech. Robot.*, vol. 3, no. 2, pp. 1–10, May 2011.

[24] R. Babaghasabha, M. A. Khosravi, and H. D. Taghirad, "Adaptive robust control of fully-constrained cable driven parallel robots," *Mechatronics*, vol. 25, pp. 27–36, Feb. 2015.

[25] D. B. Camarillo, C. F. Milne, C. R. Carlson, M. R. Zinn, and J. K. Salisbury, "Mechanics modeling of tendon-driven continuum manipulators," *IEEE Trans. Robot.*, vol. 24, no. 6, pp. 1262–1273, Dec. 2008.

[26] S.-R. Oh and S. Agrawal, "Cable suspended planar robots with redundant cables: Controllers with positive tensions," *IEEE Trans. Robot.*, vol. 21, no. 3, pp. 457–465, Jun. 2005.

[27] M. Gouttefarde, J. Lamaury, C. Reichert, and T. Bruckmann, "A versatile tension distribution algorithm for n-DOF parallel robots driven by n+2 cables," *IEEE Trans. Robot.*, vol. 31, no. 6, pp. 1444–1457, Dec. 2015.

[28] R. J. Caverly and J. R. Forbes, "Flexible cable-driven parallel manipulator control: Maintaining positive cable tensions," *IEEE Trans. Control Syst. Technol.*, vol. 26, no. 5, pp. 1874–1883, Sep. 2018.

[29] S. K. Mustafa and S. K. Agrawal, "On the force-closure analysis of n-DOF cable-driven open chains based on reciprocal screw theory," *IEEE Trans. Robot.*, vol. 28, no. 1, pp. 22–31, Feb. 2012.

[30] W. S. Rone and P. Ben-Tzvi, "Continuum robot dynamics utilizing the principle of virtual power," *IEEE Trans. Robot.*, vol. 30, no. 1, pp. 275–287, Feb. 2014.

YA'NAN LOU received the B.S. degree in mechanical engineering from the Hefei University of Technology, Hefei, China, in 2016. He is currently pursuing the Ph.D. degree in mechanical engineering with the Harbin Institute of Technology, Harbin, China.

During his B.S. degree, he got the Honorable Mention in International Mathematical Contest in Modeling, in 2015, and acquired a Utility Model Patent named a semi-automatic machine for phone filming as the first inventor and second patent holder, in 2015. The two experiences stimulated his interest in scientific research. He is also working on cable-driven auto-charging robot for electric vehicles.

SHICHUN DI received the B.S. degree in mechanical engineering from the Dalian Railway Institute (now Dalian Jiaotong University), Dalian, China, in 1986, the M.S. and Ph.D. degrees in mechanical engineering from the Harbin Institute of Technology, Harbin, China, in 1989, and 1995, respectively.

He is currently a Professor and a Ph.D. Supervisor with the School of Mechatronics Engineering, Harbin Institute of Technology. He has successively presided over and undertook key projects of the National Natural Science Foundation, 863 key projects, a number of provincial and ministerial-level key projects and a number of international cooperation projects. With his efforts, EDM high-speed compound milling technology has been successfully applied in the production of aerospace key parts, robot technology, and, large area micro-arc oxidation treatment. His current research focuses on robotics, automatic charging robot, and intelligent three-dimensional garage.

Prof. Di has been the Vice-Chairman of Electrical Machining Branch of Chinese Mechanical Engineering Society.